

ROYAL MILITARY ACADEMY



SE511 : Strategic Military Sensors

Hyperspectral Unmixing

Officer-Student De Schamphelleire Ben

Department CISS

Under supervision of :
Prof. Neyt, Xavier
Lt. Boland, Olivier

Brussels,
December 19, 2022

Contents

1	Introduction	1
2	Used Data	2
3	Exploitation of the data	4
3.1	Extraction of the endmembers	4
3.1.1	Linear Mixing Model	4
3.1.2	Reference of the Matlab Hyperspectral Toolbox	5
3.1.3	Averaging knowing the ground truth	5
3.1.4	Methods without knowledge of the ground truth	5
3.2	Comparison of the proposed methods to the reference	8
3.3	Calculating the Covariance Matrix	11
3.4	Calculating the abundance	11
3.4.1	Method of the pseudo-inverse	11
3.4.2	Method of the optimum detection	14
3.4.3	Method of the unknown \mathbf{U}	16
4	Conclusion	21
A	Appendices	22
A.1	Field Notes Indian Pines (1992)	22
	References	24

List of Figures

1	Hyperspectral cube	1
2	Visual representation of Indian Pines, using a false coloring (left) and an RGB coloring (right)	2
3	Indian Pines ground truth	3
4	Number of endmembers in function of the PFA	6
5	Correlation of the endmembers with respect to the reference	8
6	Correlation of the endmembers with respect to the reference	8
7	Correlation of the endmembers with respect to the reference	9
8	Correlation of the endmembers with respect to the reference	9
9	Autocorrelation of reference	10
10	Abundance map of the method of the pseudo-inverse	12
11	Classification based on the method of the pseudo-inverse	13
12	Confusion matrix based on the method of the pseudo-inverse	14
13	Confusion matrix based on the method of the optimum detection	16
14	Abundance map of the method of the unknown \mathbf{U}	18
15	Classification based on the method of the unknown \mathbf{U}	19
16	Confusion matrix based on the method of the unknown \mathbf{U}	20
17	Field notes of the Indian Pines scene	22
18	Field notes of the Indian Pines scene	23

1 Introduction

When one takes a picture with a common camera, every pixel is composed of a combination of the colors red, green and blue. In order to create these so-called RGB-images, the camera needs to capture visible light (that is, visible to a human being). However, the electromagnetic spectrum extends way beyond this visible portion. Therefore, some methods have tried to collect information in other parts of the spectrum. By extension, a particular technique is commonly used for imaging purposes, where a limited spectrum of every pixel of the image is captured. This technique, called *Hyperspectral Imaging*, aims to collect a nearly-continuous spectrum of every pixel in the image, as opposed to *Multispectral Imaging*, where the sensor only captures in a few spaced spectral bands. The result of hyperspectral imaging is a collection of 2D images, each considering a different wavelength of the spectrum. This can thus be represented as a 3D image, commonly known as a hyperspectral cube, or hypercube for short. A visual representation of a hyperspectral cube is shown in the following Figure:

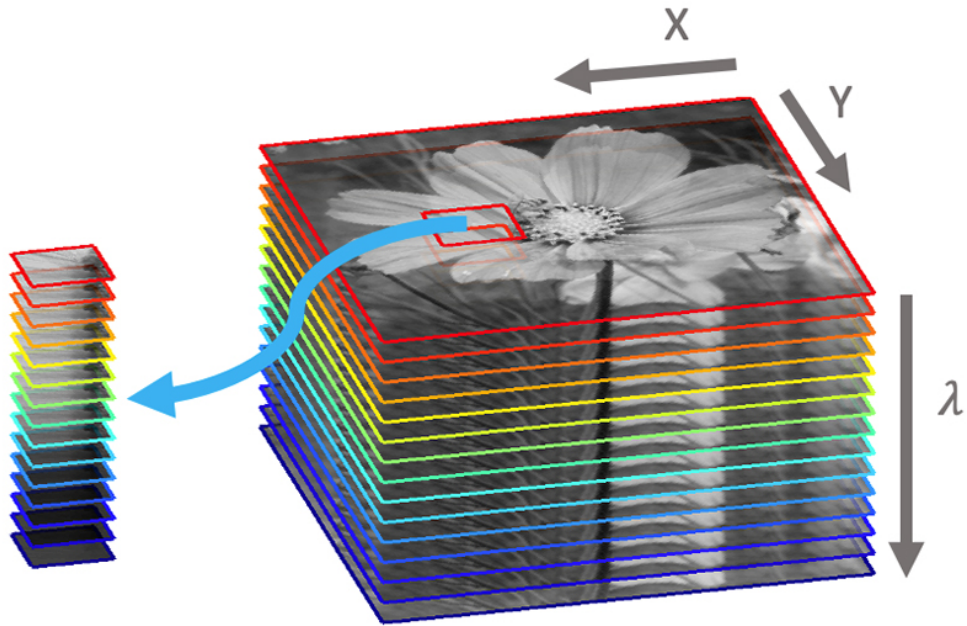


Figure 1: Hyperspectral cube

It is common knowledge that every material has a unique spectral signature. Since hyperspectral sensors use very narrow bands, the energy received for every band in a pixel is very small. To compensate for this effect, hyperspectral imagers consider large pixels. When taking a hyperspectral image, some pixels will thus contain a combination of different materials, like grass, trees, concrete, etc. Therefore, the spectrum of those pixels will contain influences of all these materials. This spectrum will also depend on numerous other factors, like the incidence angle of the illumination, aging, atmospheric effects, etc. It would be interesting to know of course what material is present in what pixel to what extent. This can be achieved with *Hyperspectral Unmixing* and will be explained in this report.

2 Used Data

Before explaining the methods to perform hyperspectral unmixing, the subjected data will first be discussed. The hyperspectral data of different scenes can be found in [8]. In this report, the scene of *Indian Pines* will be analyzed. This test-site in North-western Indiana was captured by the AVIRIS sensor [1]. The images consist of 145×145 pixels taken in 224 spectral bands in the range $400\text{nm} - 2500\text{nm}$. The scene contains mostly agricultural lands and forests as well as a handful of buildings and structures. Furthermore, the *Grupo de Inteligencia Computacional* (GIC) corrected the data in order to reduce the number of spectral bands by removing the bands corresponding to water absorption. The following bands were removed: 104 – 108, 150 – 163 and 220, resulting in 200 total bands (instead of the initial 224).

A visual representation of the scene can be found in the following Figure. On the left side, a false coloring was applied to maximize the contrast utilizing a combination of three wavelengths: 553.42 nm , 582.19 nm and 793.15 nm . On the right side, the well-known RGB-bands are depicted, as if the scene was captured with a regular camera.

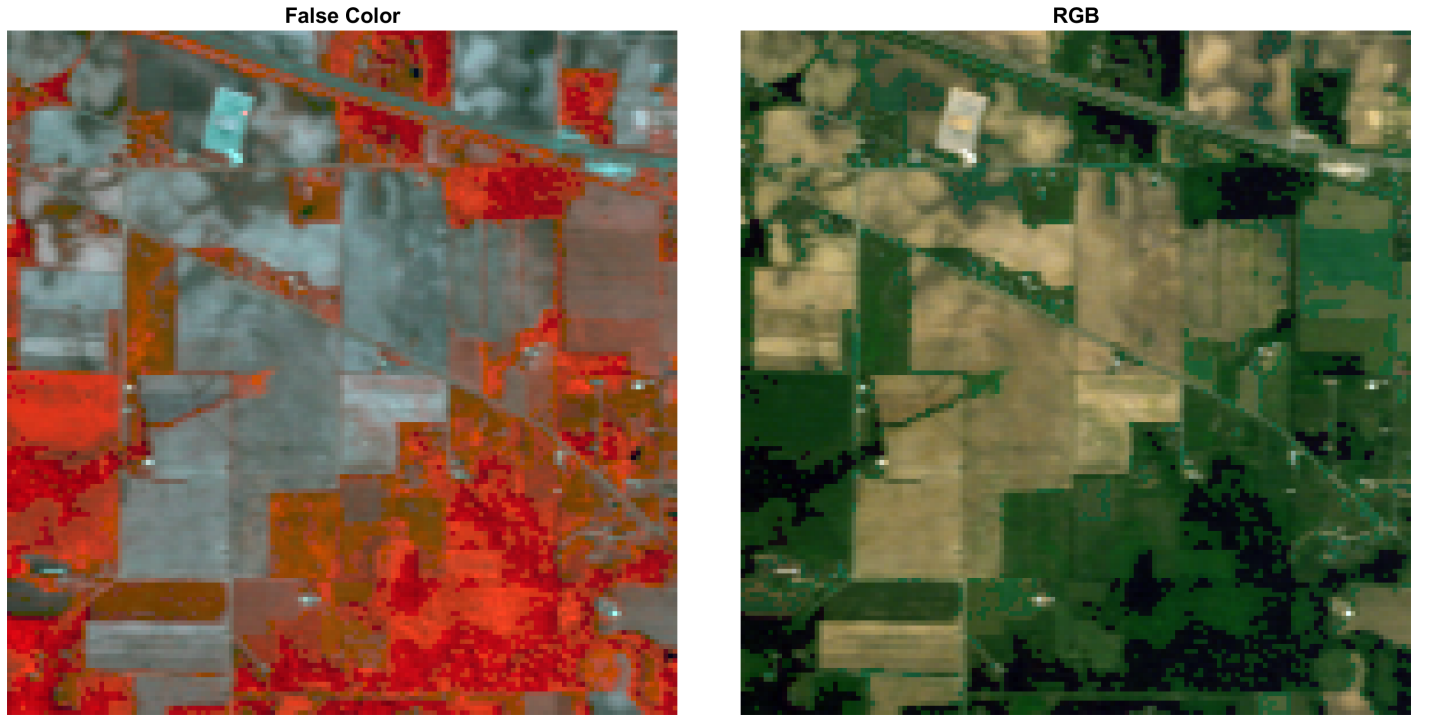


Figure 2: Visual representation of Indian Pines, using a false coloring (left) and an RGB coloring (right)

For this scene, the ground truth has been made available (the calculation process can be found in the Matlab documentation [6]). It contains 16 classes and is visually represented in the Figure 3 below. Note that the colors are not realistic but are chosen to maximize the contrast and thus augment the readability.

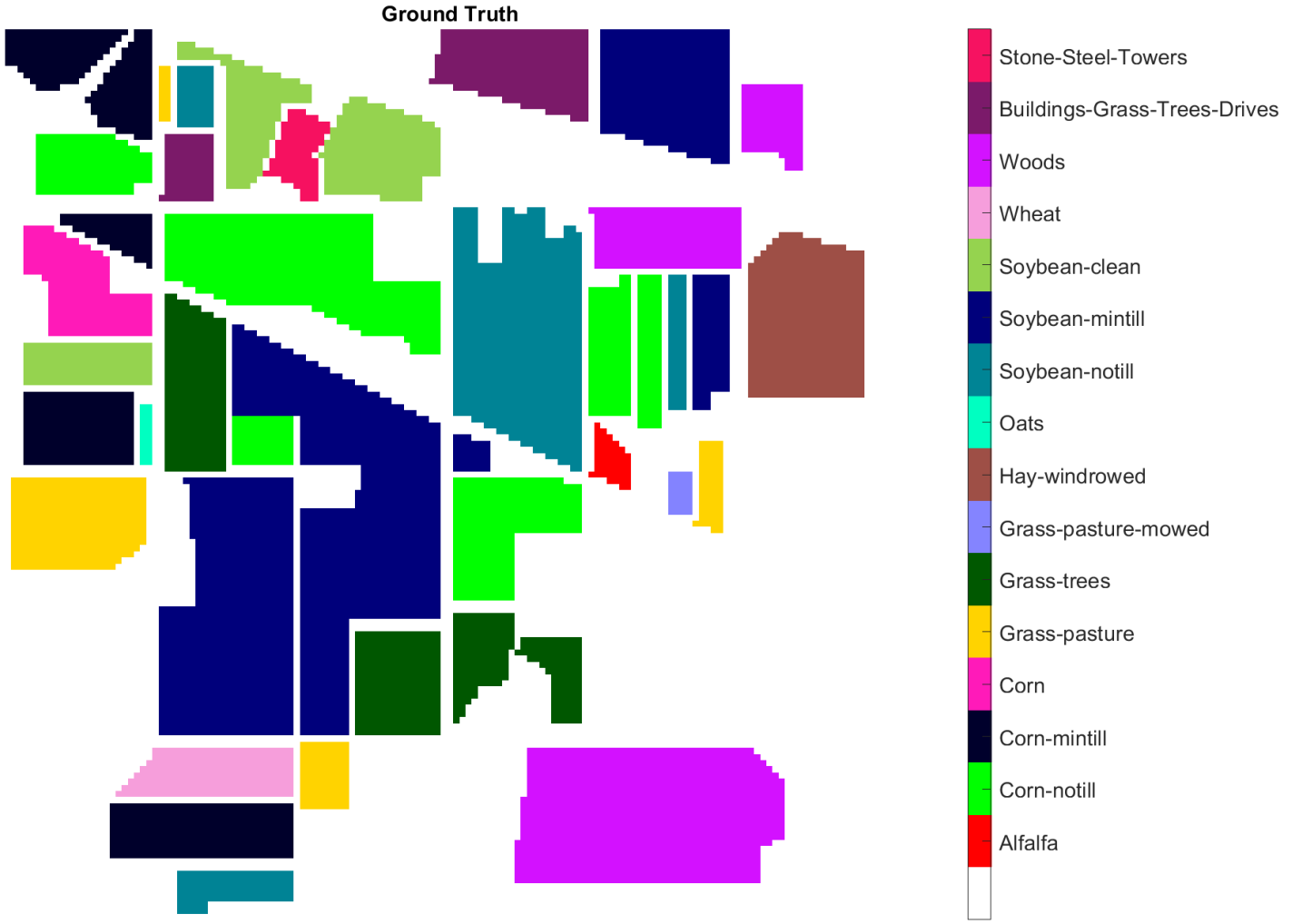


Figure 3: Indian Pines ground truth

As can be seen, the scene mostly contains crops and forest with some buildings and constructions to a small extent. Interesting to note is that the ground truth also contains pixels that do not belong to one of the 16 classes (depicted in white). This does not imply the absence of those classes in these zones, as can be seen on the illustrations in Appendix A.1. These notes were created during the measurement campaign in 1992 and clearly show that the empty zones on the ground truth do contain some traces of the classes. Nevertheless, this ground truth will serve as a reference in this report.

3 Exploitation of the data

As explained in the introduction, the aim of this project is to perform hyperspectral unmixing in order to detect which materials are present in which pixels and to what degree. The corresponding code and the images can be found on the following GitHub repository [7].

3.1 Extraction of the endmembers

Since the spatial resolution of a hyperspectral sensor is limited, a single pixel will contain reflections from several objects. The spectral signatures of those different objects will all influence the spectrum of said pixel. Therefore, one needs to determine to what extent a certain object is present in a pixel. For this, a *Linear Mixing Model* will be used in this project.

3.1.1 Linear Mixing Model

The Linear Mixing Model assumes the reflectance of a pixel is the result of the weighted sum of the reflectances of the different objects in the pixel.

Let k be a certain material and L be the number of considered spectral bands, then

$$\mathbf{m}_k = [m_k(\lambda_1), m_k(\lambda_2), \dots, m_k(\lambda_L)]^T \quad (1)$$

is the spectral signature of material k and is called the *endmember* of material k .

One can also note the measurement at a particular pixel, corresponding to the reflectance of that pixel for the different spectral bands:

$$\mathbf{r} = [r_1, r_2, \dots, r_L]^T \quad (2)$$

Using this notation, the Linear Mixing Model can be expressed as follows:

$$\mathbf{r} = \sum_{k=1}^p \alpha_k \mathbf{m}_k + \mathbf{n} \quad (3)$$

with p being the number of different materials present in the particular pixel. The coefficients of the linear combination indicate to what degree a particular material is present in the considered pixel and is called the *abundance* of said material. The vector \mathbf{n} contains the noise.

The equation (3) can be rewritten in matrix form:

$$\mathbf{r} = \mathbf{M}\boldsymbol{\alpha} + \mathbf{n} \quad (4)$$

with $\mathbf{M} = [\mathbf{m}_1, \mathbf{m}_2, \dots, \mathbf{m}_p]$ and $\boldsymbol{\alpha} = [\alpha_1, \alpha_2, \dots, \alpha_p]^T$.

Note that, in reality, the measurements \mathbf{r} are available and that the different endmembers \mathbf{M} may be fully or only partially known. Based on the previous equation, performing hyperspectral unmixing comes down to determining the different α_k ($0 \leq \alpha_k \leq 1$) for the materials one is interested in.

3.1.2 Reference of the Matlab Hyperspectral Toolbox

The data of the Indian Pines scene is also freely available from the *Hyperspectral Toolbox* and contains the hypercube of the scene, the different wavelengths considered as well as the signature of 16 endmembers. For the remainder of this project, this will be considered as the reference, since those data were used to construct the ground truth through Machine Learning [6].

3.1.3 Averaging knowing the ground truth

One possible method to extract the different endmembers is to take an average of all the spectral signatures of the pixels based on their class in the ground truth. This method requires of course the knowledge of this ground truth and is not always a feasible solution.

3.1.4 Methods without knowledge of the ground truth

Alternatively, one could consider the extraction of endmembers without a priori knowledge of the ground truth. Three such methods are described in the following paragraphs. Note that every method has at least one parameter whose influence can be studied. Given the nature of this project, a choice has been made not to analyze the influence of the different parameters on the calculation of the endmembers. Instead, Matlab's default parameters were used.

Noise-whitenend Harsanyi–Farrand–Chang (HFC)

The three methods that follow do not need to know the ground truth in order to calculate the endmembers, but they all require (an estimation of) the amount of endmembers that should be extracted. To this end, the Harsanyi–Farrand–Chang (HFC) approach is used. If one considers Noise Whitening, then the only parameter to investigate is the Probability of a False Alarm (PFA). This parameter roughly corresponds to the probability that a particular eigenvalue of the correlation matrix is equal to the corresponding eigenvalue of the covariance matrix. In this case, no endmember contributes to the eigenvalue of the correlation matrix, the only contribution stems from noise. The influence of this parameter is represented in the following Figure.

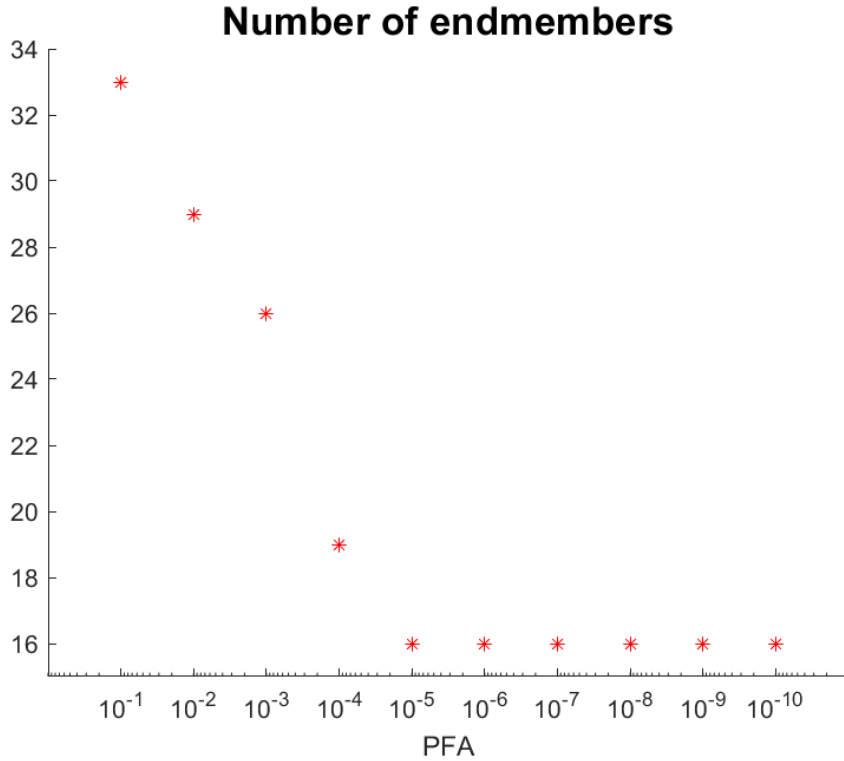


Figure 4: Number of endmembers in function of the PFA

One can observe that smaller values of the PFA lead to fewer endmembers. This makes sense since a smaller value of the PFA implies that there is often an existing endmember contributing to the eigenvalues of the correlation matrix in addition to noise, meaning that the possible total number of endmembers will be smaller. One can also notice that the number of endmembers stabilizes for values of the PFA smaller than or equal to 10^{-5} . Moreover, the estimated number of endmembers in this case corresponds to the number of endmembers in the reference data. These observations allow to validate the noise-whitenend HFC method, on condition that the PFA is chosen to be small enough.

Pixel Purity Index (PPI)

Now that the number of endmembers is determined without the a priori knowledge of the ground truth, this information can be used to calculate the different endmembers present in the scene. A first method is called the Pixel Purity Index (PPI, [2] [11]), which projects the hyperspectral data on a set of randomly generated unit vectors (called skewers). Then, the number of times the spectrum of a certain pixel results in an extremum after projection (i.e. when the pixel's spectrum falls at the ends of the unit vector) is counted. This count corresponds to the Pixel Purity Index. After that, the n spectra of the pixels with the highest PPI count are taken as the endmembers, with n the number of desired endmembers. The method allows to specify two parameters, the number of random unit vectors to use for the projection as well as the used dimensionality reduction method. As explained before, the default parameters of this method will be considered, being 10^4 vectors and the Maximum Noise Fraction (MNF) method, respectively. This technique allows to determine the endmembers, but a major drawback of the algorithm is the computational complexity. Since the Indian Pines scene is rather small (145×145), the computational requirements remain limited, but for larger scenes this quickly becomes a burden. The

complexity is somewhat mediated by the addition of a dimensionality reduction method, but still the computation time is a bottleneck. Another inconvenience lies in the randomly generated unit vectors, which influence the result. In other words, a different set of unit vectors can lead to a different result for the endmembers. Finally, since the process is not iterative, it does not guarantee convergence of the calculated endmembers.

N-FINDR

A second approach that is commonly used to determine the endmembers is called N-FINDR [12]. This method is based on the principle that in N spectral dimensions, the N -dimensional volume of a simplex composed of the purest pixels is always larger than any other volume composed of any other combination of pixels. This theory is applied as follows. First, a random set of pixels is chosen as a starting configuration. Then, for every pixel and every endmember in the simplex, the spectrum of this pixel is swapped for the endmember in the simplex and the N -dimension volume of the simplex is recalculated. If the new N -dimension volume of the simplex is larger, then the spectrum of the considered pixel will take the place of the considered endmember in the simplex. This iterative process is then repeated until no more swapping can be done. This approach allows to specify two parameters, the number of iterations and the used dimensionality reduction method. Once again, the Matlab's default values will be considered. In this case, this corresponds to $3 \cdot N$ iterations (with N the number of endmembers to be extracted) and the Maximum Noise Fraction (MNF), respectively. Even though this method allows to calculate the different endmembers, there is one major disadvantage. Randomly chosen initial endmembers are used, which leads to inconsistent results in finding endmembers. For instance, a different set of random initial endmembers could result in a different set of extracted endmembers [13].

Fast Iterative PPI (FIPPI)

The last technique detailed in this project is based on the PPI method, but aims to improve its computational complexity. Therefore, it is called Fast Iterative PPI (FIPPI, [5]). Since this method is iterative, one can evaluate the convergence of the calculated endmembers, as opposed to the PPI approach. Moreover, the FIPPI uses an Automatic Target Generation Process (ATGP) to determine an appropriate initial set of endmembers, which takes away the influence of a random choice and thus make the algorithm reproducible. Instead of calculating the projections of every pixel's spectrum on all skewers, the FIPPI iteratively calculates the projection of all pixel's spectra on only one skewer. Then an ensemble of the pixel's spectra leading to an extremum is created (i.e. when the pixel's spectrum falls at the ends of the unit vector). At the next iteration, and thus after projection on another skewer, if the ensemble of pixel's spectra hasn't changed, the process is completed and the ensemble will contain the extracted endmembers. Therefore, the method converges very rapidly and is thus generally faster than the PPI. The FIPPI algorithm removed the need to specify the number of unit vectors in advance (like is the case for the PPI method) and thus only requires the choice of a dimensionality reduction method. By default, the Maximum Noise Fraction (MNF) is used and thus it will also be used in this project. Of course, there is no free lunch. The reduced computational complexity of the algorithm negatively impacts its precision. Depending on the convergence criterion, the calculated set of endmembers could converge while the number of endmembers does not correspond to the desired number.

3.2 Comparison of the proposed methods to the reference

Now that methods for extracting the endmembers are detailed, their results will be compared to the endmembers of the reference by calculating the correlation. The values of the correlation are visually represented in the following Figures.

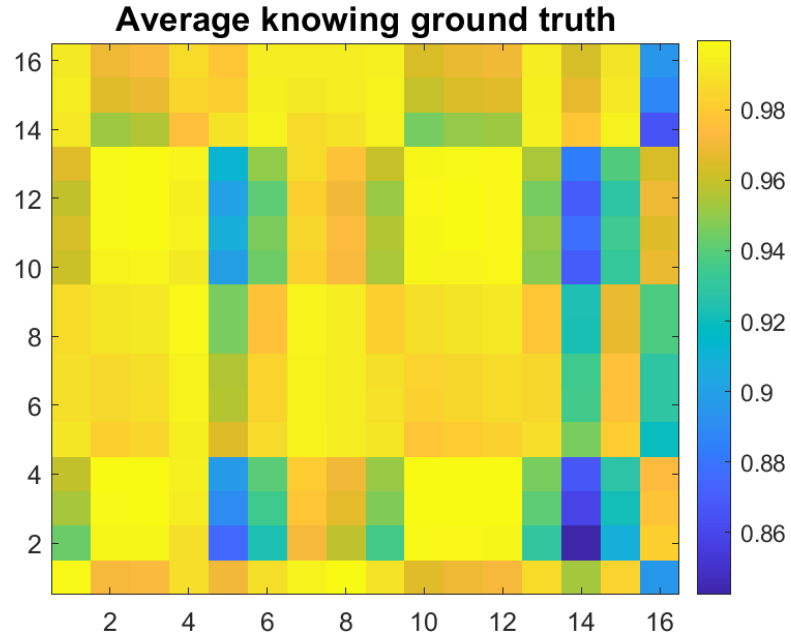


Figure 5: Correlation of the endmembers with respect to the reference

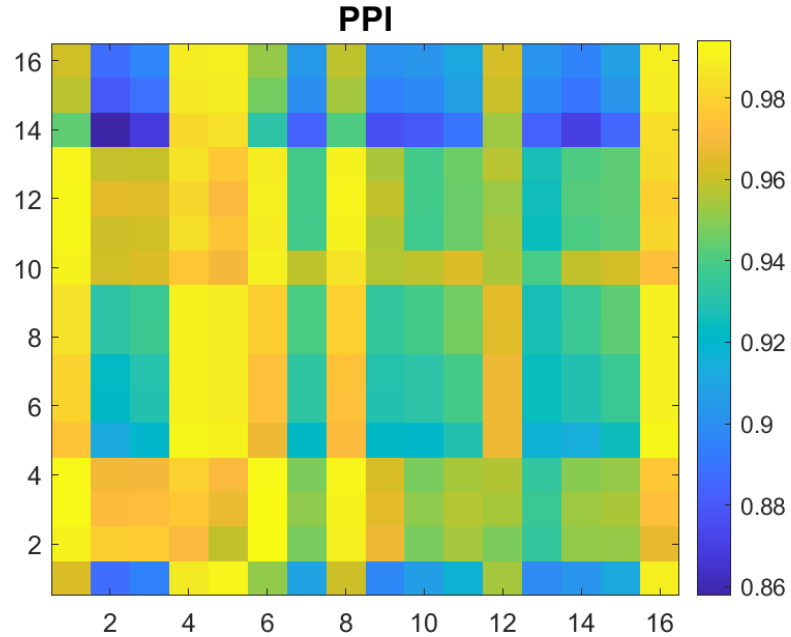


Figure 6: Correlation of the endmembers with respect to the reference

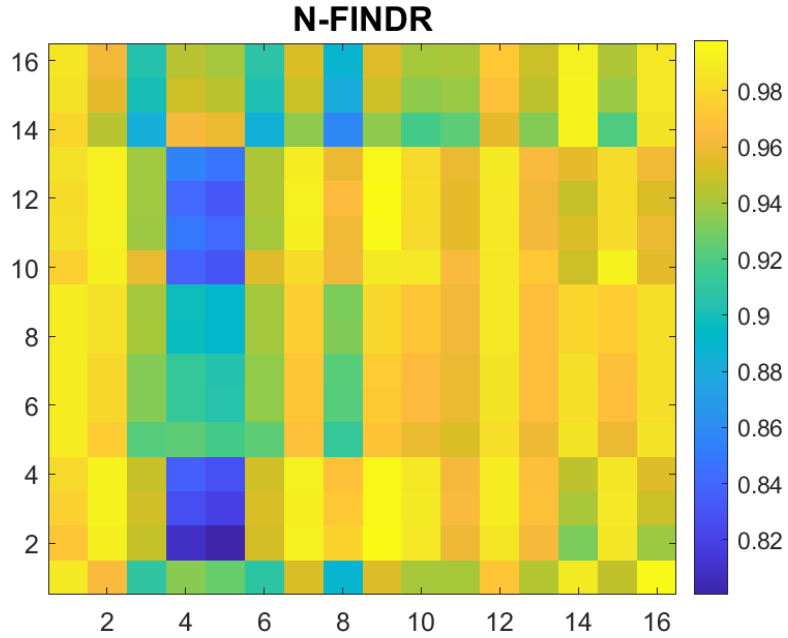


Figure 7: Correlation of the endmembers with respect to the reference

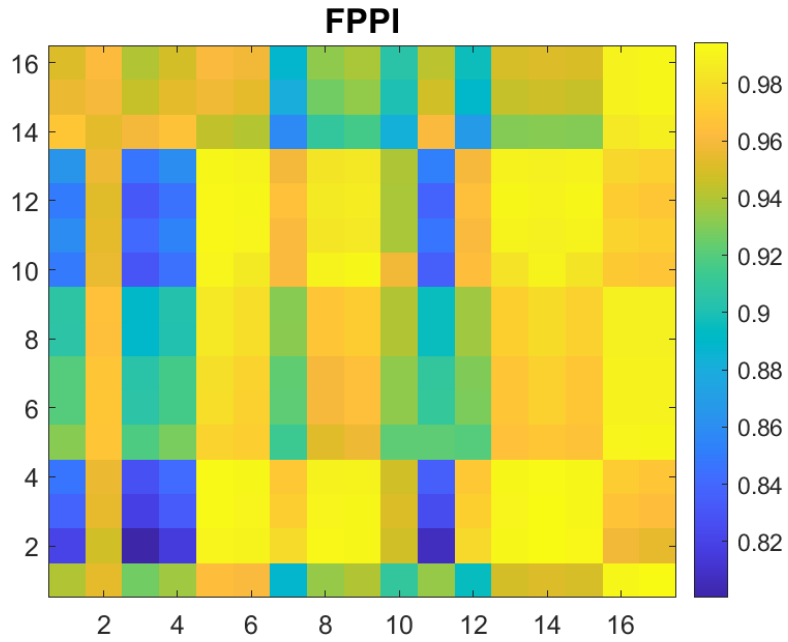


Figure 8: Correlation of the endmembers with respect to the reference

The results should be interpreted as follows. The vertical axis always ties to the endmembers of the reference, while the horizontal axis contains the endmembers of the particular method. For instance, the value at the position (2 up, 4 right) corresponds to the correlation between the second endmember of the reference and the fourth endmember of one of the four methods. One would thus expect the values on the diagonal of every plot to be maximal. However, the different methods calculate the endmembers

in their unique way. Consequently, there is no guarantee that the endmembers are listed in the same order for every method.

Several interesting conclusions can be made nevertheless. First and foremost, one immediately notices the FPPI approach generates 17 endmembers instead of the desired 16. This is due to the preliminary convergence of the iterative method, as explained in the previous section. Moreover, when looking at each row of the different Figures (and thus at one particular endmember of the reference), one would expect a single value to be significantly larger than the others of said row. This would then indicate the corresponding endmember calculated by the method. However, when looking at all four Figures, no such phenomenon can be noticed. Instead, multiple endmembers correlate significantly to a particular endmember of the reference, always with a minimum correlation of 80%! Besides, when looking at the columns, one can verify that a certain endmember calculated by the method correlates significantly to multiple endmembers of the reference. The combination of these two effects and thus the fact that the correlation is high in general does not allow to link the calculated endmembers to those of the reference based on correlation.

A possible explanation resides in the inherent correlation of the endmembers of the reference, as shown in following Figure.

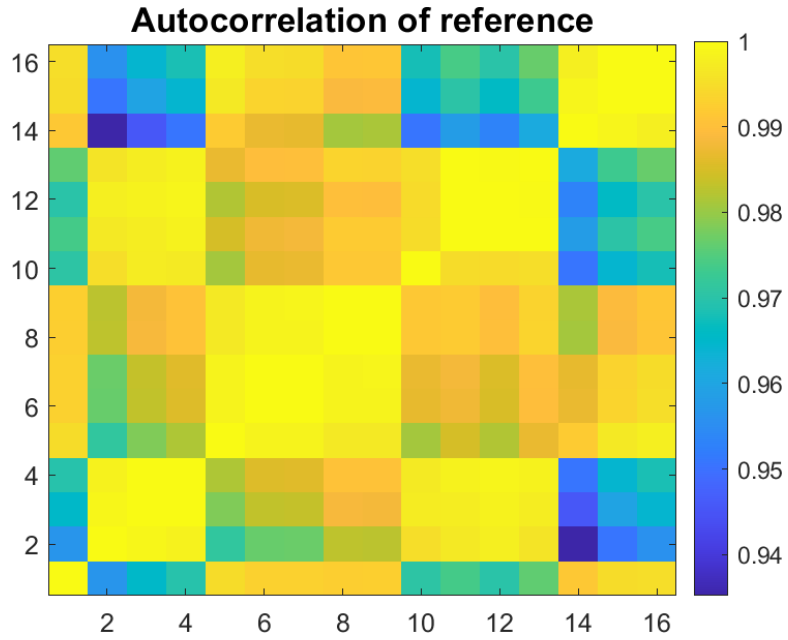


Figure 9: Autocorrelation of reference

As can be noticed, certain endmembers of the reference are highly correlated to each other. In conclusion, the use of correlation as a metric is not a valid choice when evaluating the calculated endmembers of the different methods. Therefore, for the remainder of this report, the calculated endmembers based on the knowledge of the ground truth will be used, since these are assumed to be the most reliable because of their relation to the ground truth. Note than another possible option to verify the endmembers of each method would be to use these endmembers for the calculation of the abundance and evaluating the correspondence to the ground truth. However, since the nature of this project, this is omitted from the report.

3.3 Calculating the Covariance Matrix

Before continuing with the calculation of the abundance, the covariance matrix of the different pixel's spectra is calculated. This is done based on the following equation:

$$\mathbf{R} = \frac{1}{K} \sum_{k=1}^K \mathbf{r}_k \mathbf{r}_k^T \quad (5)$$

with K the total number of pixels per spectral band (so the total number of pixels per image at a certain wavelength, 145^2 in this case).

3.4 Calculating the abundance

Now, the calculation of the abundance for every endmember will be detailed. Three methods for calculating the abundance will be discussed.

3.4.1 Method of the pseudo-inverse

For this first approach, the matrix \mathbf{M} containing the endmembers is assumed to be known. Then, the abundance can be calculated based on equation (4) by applying the least squares algorithm.

$$\hat{\boldsymbol{\alpha}} = \underset{\boldsymbol{\alpha}}{\operatorname{argmin}} \| \mathbf{r} - \mathbf{M}\boldsymbol{\alpha} \|^2 \quad (6)$$

When optimizing this problem (minimizing the cost function $\| \mathbf{r} - \mathbf{M}\boldsymbol{\alpha} \|^2$, one easily finds a solution for the abundance.

$$\hat{\boldsymbol{\alpha}} = (\mathbf{M}^T \mathbf{M})^{-1} \mathbf{M}^T \mathbf{r} \quad (7)$$

Note that the calculation of the pseudo-inverse requires $\mathbf{M}^T \mathbf{M}$ to be invertible, meaning that the columns of this matrix (and thus the endmembers) should be linearly independent.

After implementing this method, the abundances were plotted on a so-called *Abundance Map*.

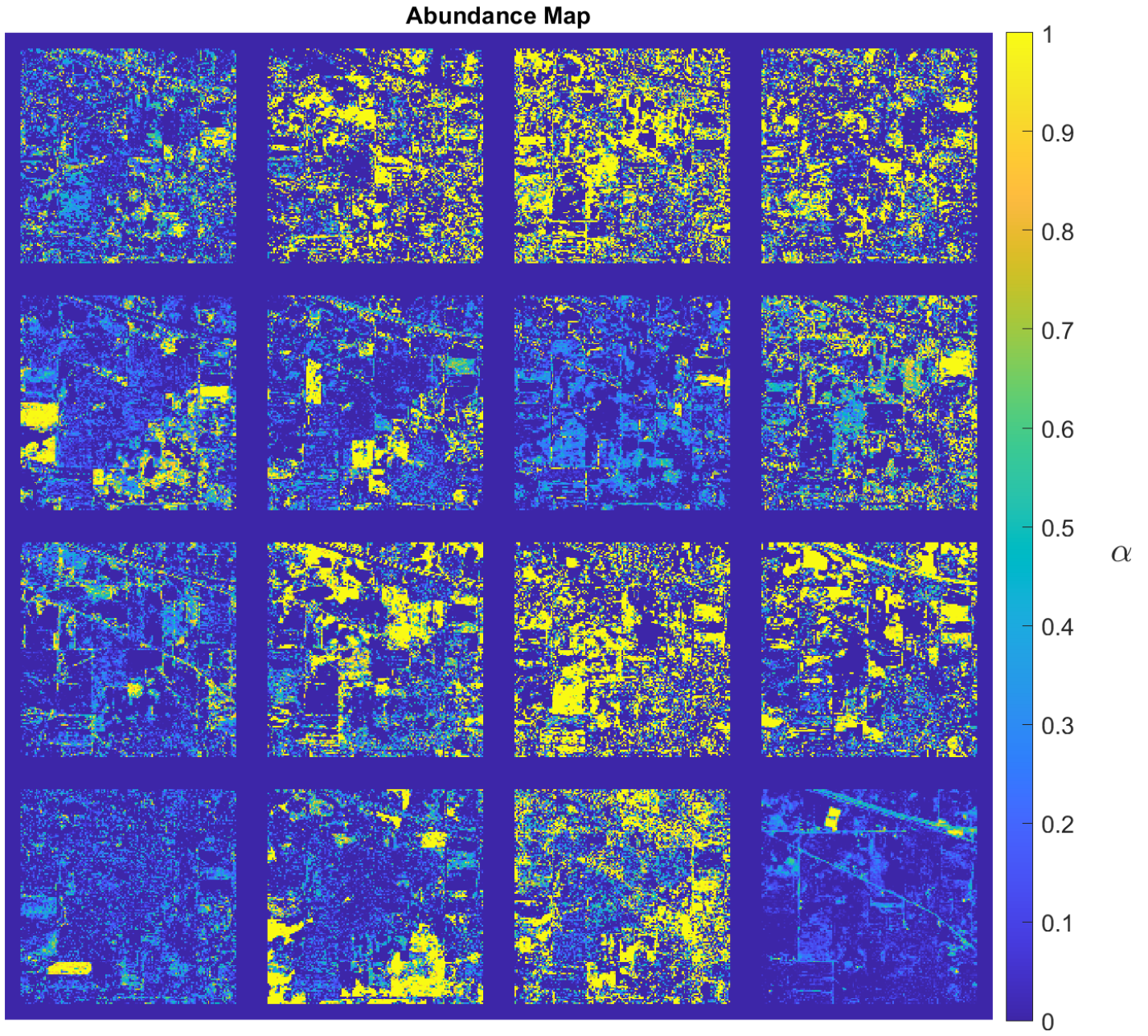


Figure 10: Abundance map of the method of the pseudo-inverse

One can immediately see that for several endmembers, the abundance is very high (sometimes maximal) on plenty of locations. Conversely, some locations in the image contain very high abundances for multiple endmembers. This is due to multiple reasons. First, the endmembers were assumed to be linearly independent. However, when calculating the determinant of $\mathbf{M}^T \mathbf{M}$, a value of $5.7472 \cdot 10^{96}$ is found and not 0. This implies that the endmembers are not spectrally independent at all. Secondly, because the abundance is limited between 0 and 1, the calculated values were manually set to these limits when the value was either smaller than 0 or larger than 1. This introduces rounding errors and consequently adds noise to the abundances.

Using the calculated abundances, a classification is performed based on the maximum abundance per pixel (before rounding to 0 or 1 if necessary). The corresponding endmember is then assumed to be dominantly present in said pixel. The result of this classification algorithm is shown in the following Figure.

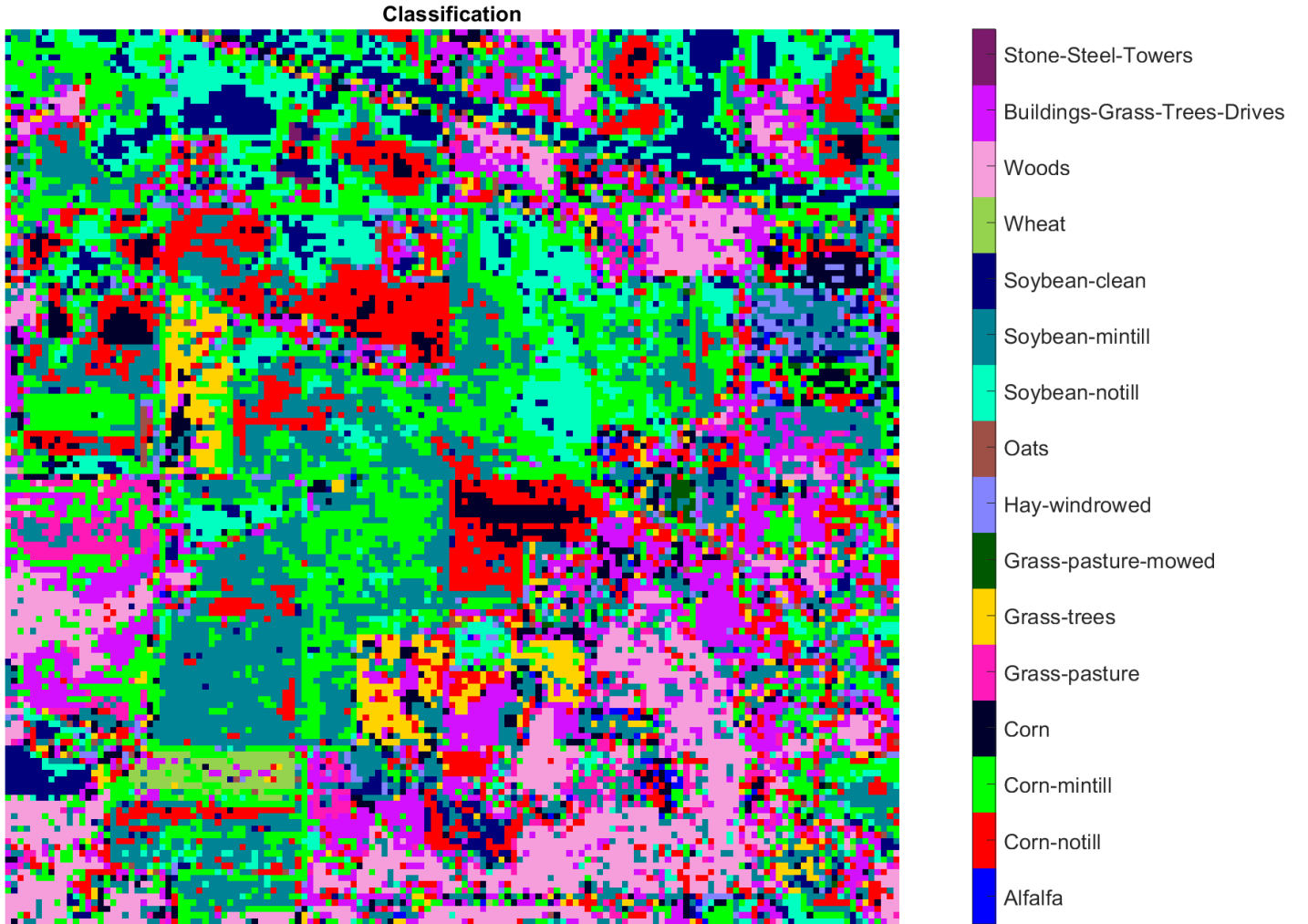


Figure 11: Classification based on the method of the pseudo-inverse

One can immediately see that the classification varies strongly from pixel to pixel and that only a handful of zones contain neighboring pixels with the same classification. This hints that the classification is not very truthful, but one can of course never be sure based solely on visual confirmation. Therefore, the classification is compared to the ground truth by creating a *Confusion Matrix*.

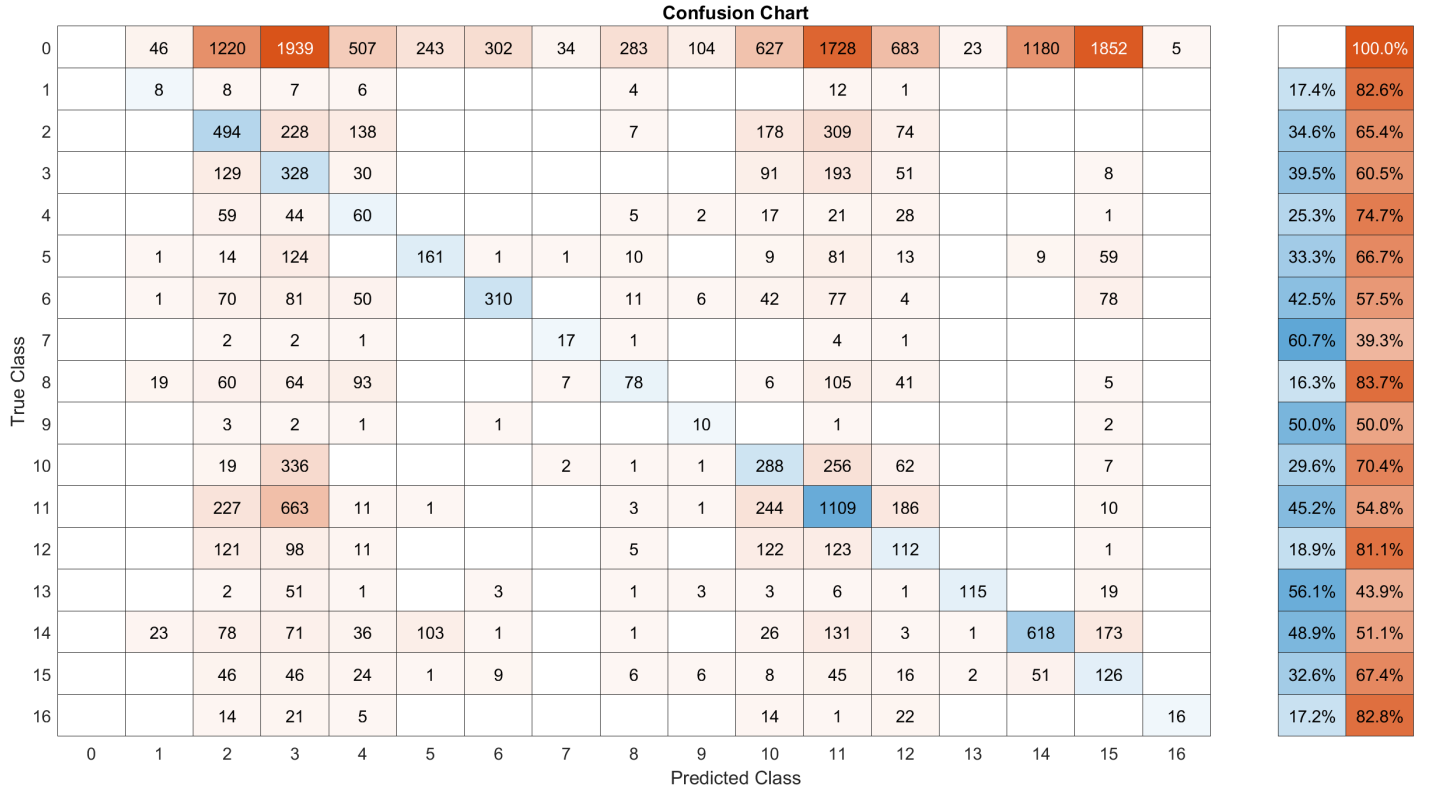


Figure 12: Confusion matrix based on the method of the pseudo-inverse

In the matrix, it can be seen that the first column is completely zero. This is easily explained by the fact that the ground truth contains a class 0, while this class will of course never be predicted by the algorithm. Following the same reasoning, the explanation for the high values in the first row is straightforward. The algorithm will never predict a pixel to belong to class 0, so the pixels of the ground truth belonging to this class will never be correctly classified. This is not a problem as such, one should solely focus on the classification of the other classes. In order to augment the readability, a summarizing table was added to the plot. On this table, one can see the correct or false predictions per class of the ground truth. In order words, it shows how often a certain class of the ground truth was correctly identified as such. The table shows that the classification is not very successful for all classes. Again, this is due to the imprecision of the calculated abundances.

3.4.2 Method of the optimum detection

Alternatively, one could use a second approach, called the method of optimum detection. The aim of this technique is to calculate the abundance of one particular endmember $\mathbf{d} = \mathbf{m}_p$. The equation (4) can then be rewritten as follows:

$$\mathbf{r} = \alpha_p \mathbf{d} + \mathbf{U} \boldsymbol{\alpha}' + \mathbf{n} \quad (8)$$

with $\mathbf{U} = [\mathbf{m}_1, \mathbf{m}_2, \dots, \mathbf{m}_{p-1}]$ and $\boldsymbol{\alpha}' = [\alpha_1, \alpha_2, \dots, \alpha_{p-1}]^T$.

One can then estimate $\boldsymbol{\alpha}'$ using the method of the pseudo-inverse:

$$\hat{\alpha}' = (\mathbf{U}^T \mathbf{U})^{-1} \mathbf{U}^T \mathbf{r} \quad (9)$$

By extracting the contributions of the other undesired endmembers:

$$\mathbf{r} - \mathbf{U} \hat{\alpha}' = \left(\mathbf{I} - \mathbf{U} (\mathbf{U}^T \mathbf{U})^{-1} \mathbf{U}^T \right) \mathbf{r} = \mathbf{P}_U^\perp \mathbf{r} \quad (10)$$

One can simplify the equation (8), since $\mathbf{P}_U^\perp \mathbf{U} = 0$

$$\mathbf{P}_U^\perp \mathbf{r} = \alpha_p \mathbf{P}_U^\perp \mathbf{d} + \mathbf{P}_U^\perp \mathbf{n} \quad (11)$$

The previous equation then allows to estimate α_p using the approach of the least squares.

$$\hat{\alpha}_p = \underset{\alpha_p}{\operatorname{argmin}} \| \mathbf{P}_U^\perp \mathbf{r} - \alpha_p \mathbf{P}_U^\perp \mathbf{d} \|^2 \quad (12)$$

and thus

$$\hat{\alpha}_p = \frac{\mathbf{d}^T \mathbf{P}_U^\perp \mathbf{r}}{\mathbf{d}^T \mathbf{P}_U^\perp \mathbf{d}} \quad (13)$$

This approach differs from the method of the pseudo-inverse in the sense that it requires an iterative calculation over the different endmembers, while the pseudo-inverse allows to directly calculate the abundance for all endmembers at once. Other than that, the two methods consider the same assumptions and are thus completely equivalent.

Under the assumption that both methods produce the same results, only the confusion matrix will be shown. This allows to better compare results with respect to visually comparing the abundance map or classification image.

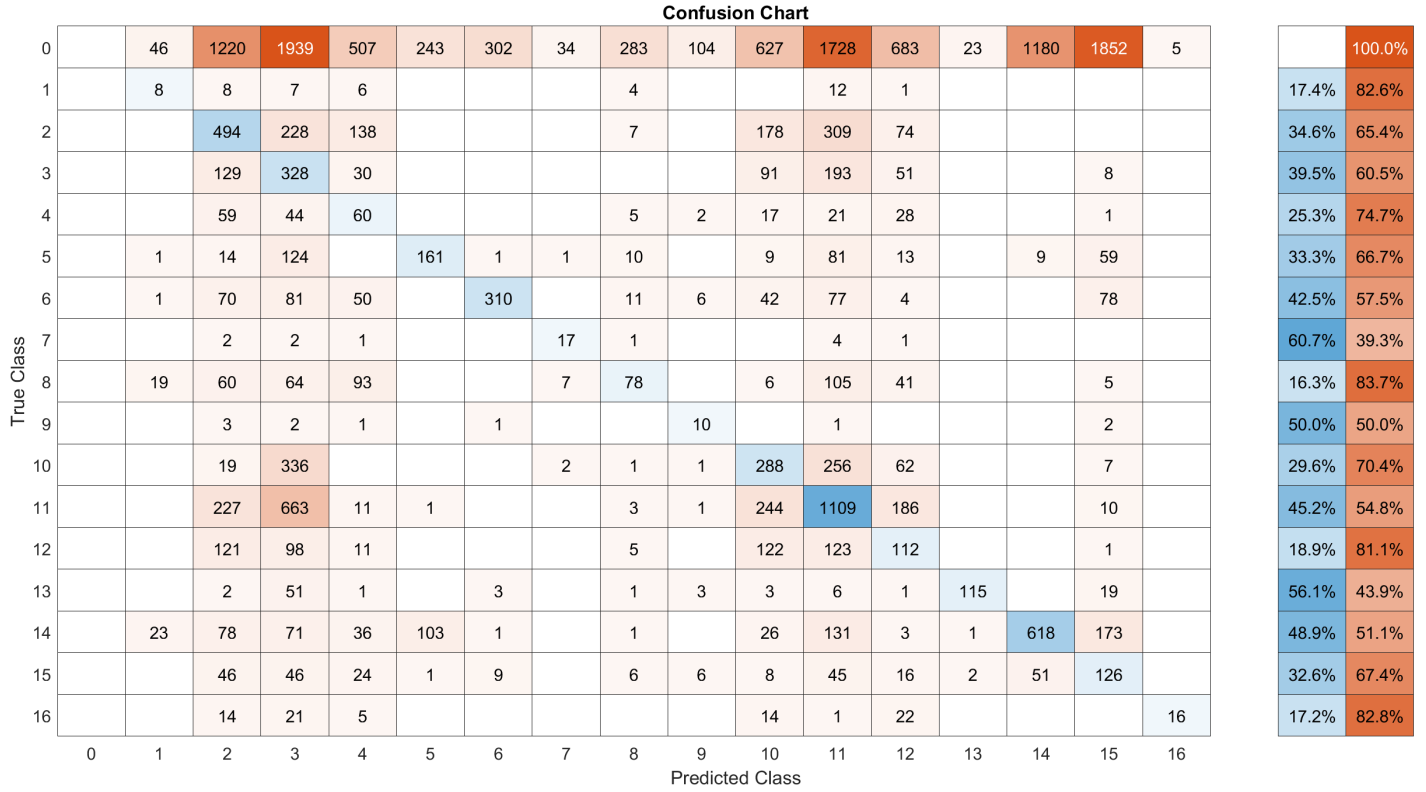


Figure 13: Confusion matrix based on the method of the optimum detection

As can be seen, the confusion matrix is completely equivalent to the confusion matrix of the previous method (Figure 12). Therefore, it is proven that both methods are completely equivalent. In this case, the abundance map and classification image will be exactly the same and will not be shown again in this paragraph. Moreover, the same conclusions apply for both methods, so they will not be repeated here.

3.4.3 Method of the unknown \mathbf{U}

The last method that will be evoked is based on the method of the optimum detection, as described in the previous paragraph. However, instead of assuming all the endmembers are known, only the desired endmember is assumed to be known. The solution to this problem comes down to designing a filter \mathbf{w} such that the energy of the filtered signal is minimized:

$$\frac{1}{K} \sum_{k=1}^K \|\mathbf{w}^T \mathbf{r}_k\|^2 = \left(\frac{1}{K} \mathbf{w}^T \sum_{k=1}^K \mathbf{r}_k \mathbf{r}_k^T \right) \mathbf{w} = \mathbf{w}^T \hat{\mathbf{R}} \mathbf{w} \quad (14)$$

Of course, the considered endmember should not be attenuated

$$\mathbf{w}^T \mathbf{d} = 1 \quad (15)$$

This approach is nothing more than an optimization problem with a given constraint, which is solved by using a Lagrange multiplier λ .

$$\mathbf{w} = \operatorname{argmin}_{\mathbf{w}} \left(\mathbf{w}^T \hat{\mathbf{R}} \mathbf{w} - 2\lambda (\mathbf{w}^T \mathbf{d} - 1) \right) \quad (16)$$

When calculating the minimum

$$\frac{\partial \left(\mathbf{w}^T \hat{\mathbf{R}} \mathbf{w} - 2\lambda (\mathbf{w}^T \mathbf{d} - 1) \right)}{\partial \mathbf{w}} = 2\hat{\mathbf{R}}\mathbf{w} - 2\lambda\mathbf{d} = 0 \quad (17)$$

And thus

$$\mathbf{w} = \lambda \hat{\mathbf{R}}^{-1} \mathbf{d} \quad (18)$$

Meaning λ has to be equal to

$$\lambda = \frac{1}{\mathbf{d}^T \hat{\mathbf{R}}^{-1} \mathbf{d}} \quad (19)$$

Finally, the filter is calculated as follows

$$\mathbf{w} = \frac{\hat{\mathbf{R}}^{-1} \mathbf{d}}{\mathbf{d}^T \hat{\mathbf{R}}^{-1} \mathbf{d}} \quad (20)$$

And the abundance can be derived as well

$$\hat{\alpha}_p = \mathbf{w}^T \mathbf{r} = \frac{\mathbf{d}^T \hat{\mathbf{R}}^{-1} \mathbf{r}}{\mathbf{d}^T \hat{\mathbf{R}}^{-1} \mathbf{d}} \quad (21)$$

A condition to be able to use this method is that $\hat{\mathbf{R}}$ needs to be invertible. This implies that, theoretically speaking, K needs to be larger or equal than the number of endmembers p . In practice, one would want K to be far larger than p in order to get a good estimation of the eigenvalues of $\hat{\mathbf{R}}$. In the case of the Indian Pines scene, $K = 145^2$ and p equals 16. Therefore, the condition on $\hat{\mathbf{R}}$ is surely met. Once again, this method requires an iterative calculation over the different endmembers. Given the fact that a filter was designed to minimize the energy of the filtered signal (under a given constraint), the results of this approach will surely differ from the two previous approaches. Therefore, the abundance map is first shown.

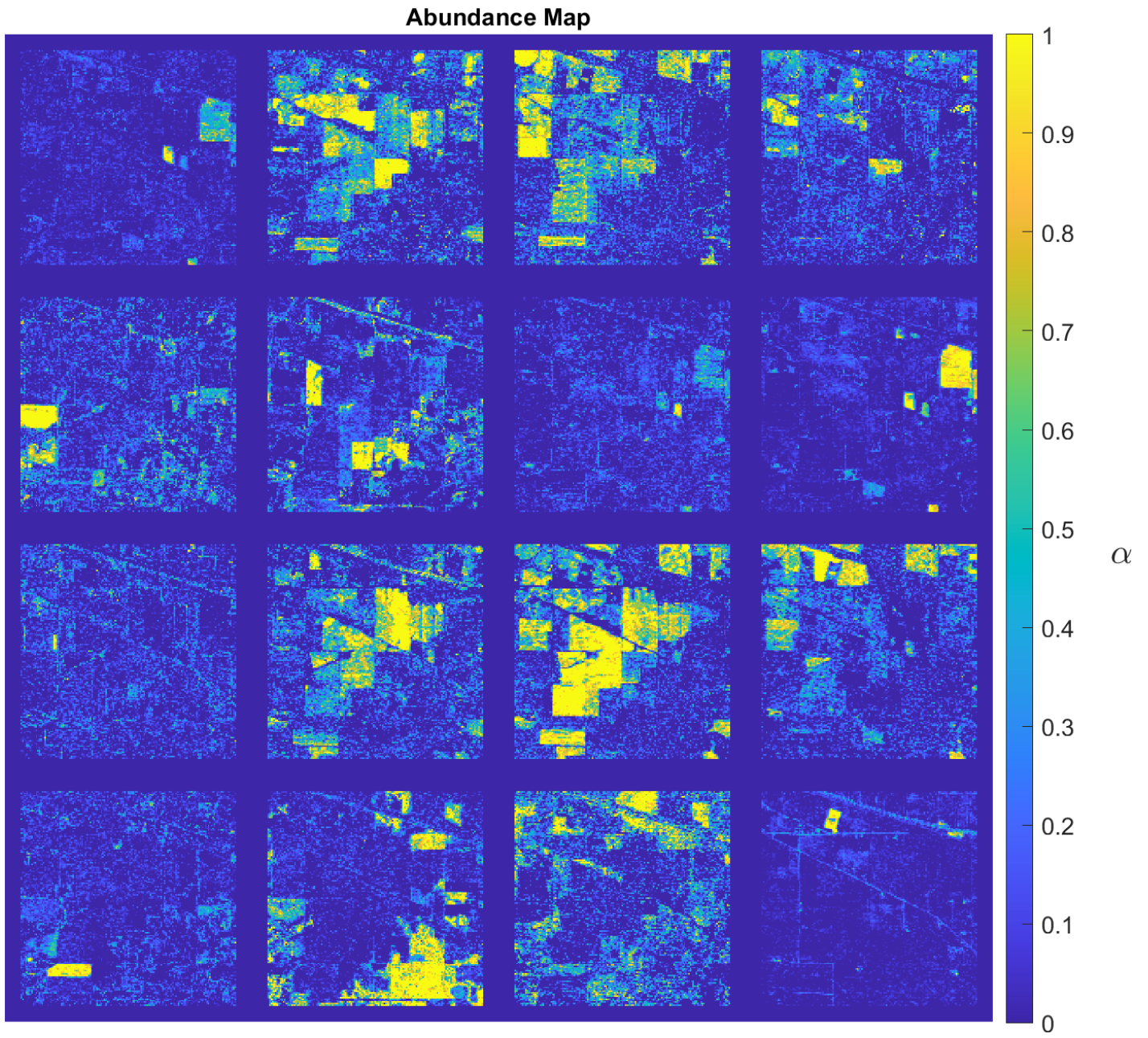


Figure 14: Abundance map of the method of the unknown \mathbf{U}

One can immediately notice that the abundances seem to correspond better to the different zones in the terrain. The abundance map looks cleaner and more realistic. Based on these abundances, every pixel is classified based on the maximum abundance. The result of the classification is represented in the following Figure.

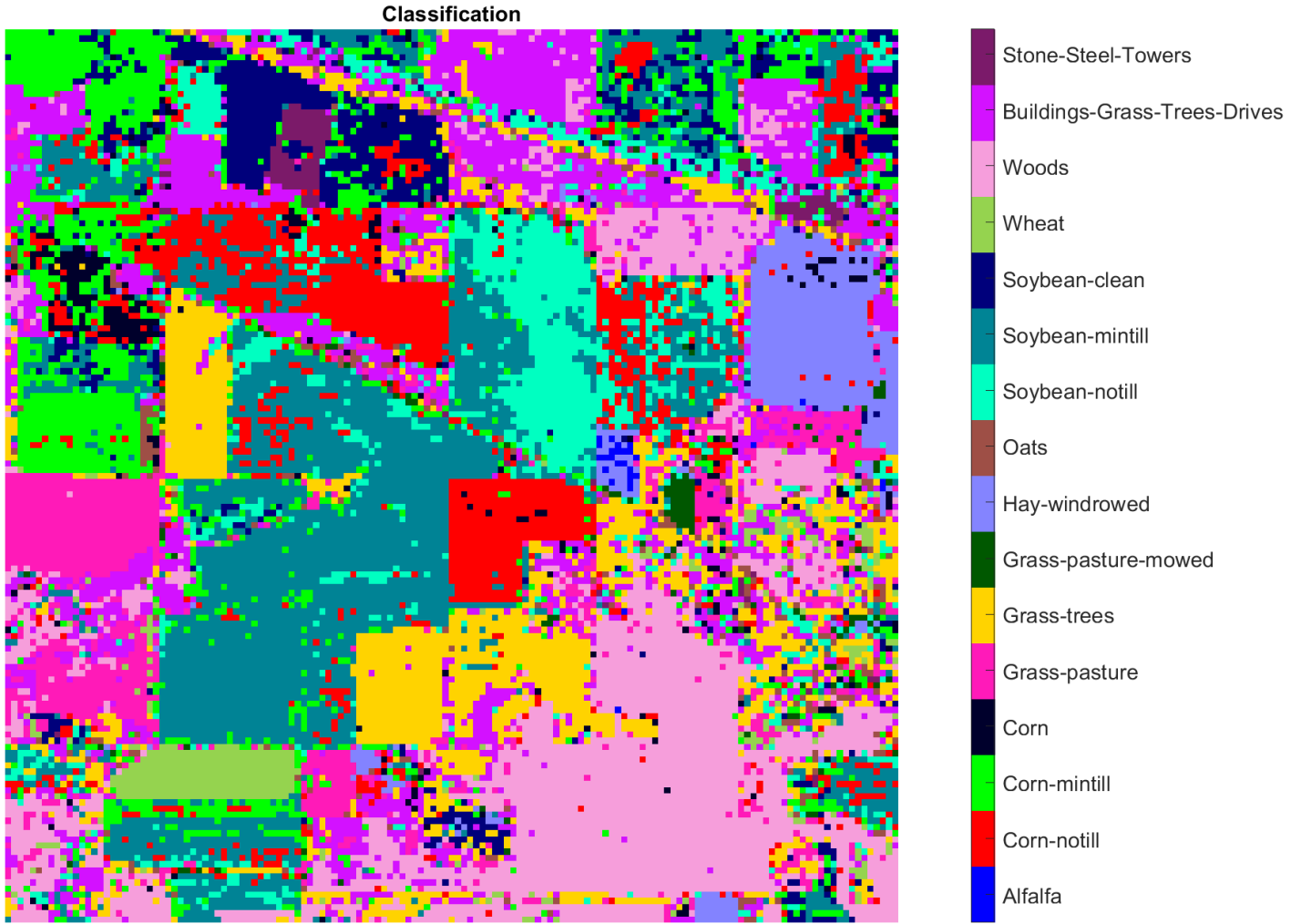


Figure 15: Classification based on the method of the unknown \mathbf{U}

After comparison to the classification of the two previous methods (Figure 11), the result seems more truthful and realistic, indicating some coherent zones instead of the individually classified pixels before. Of course, visual inspection of the abundance map and classification image does not allow to objectively evaluate a certain method. To this end, the confusion matrix is represented.

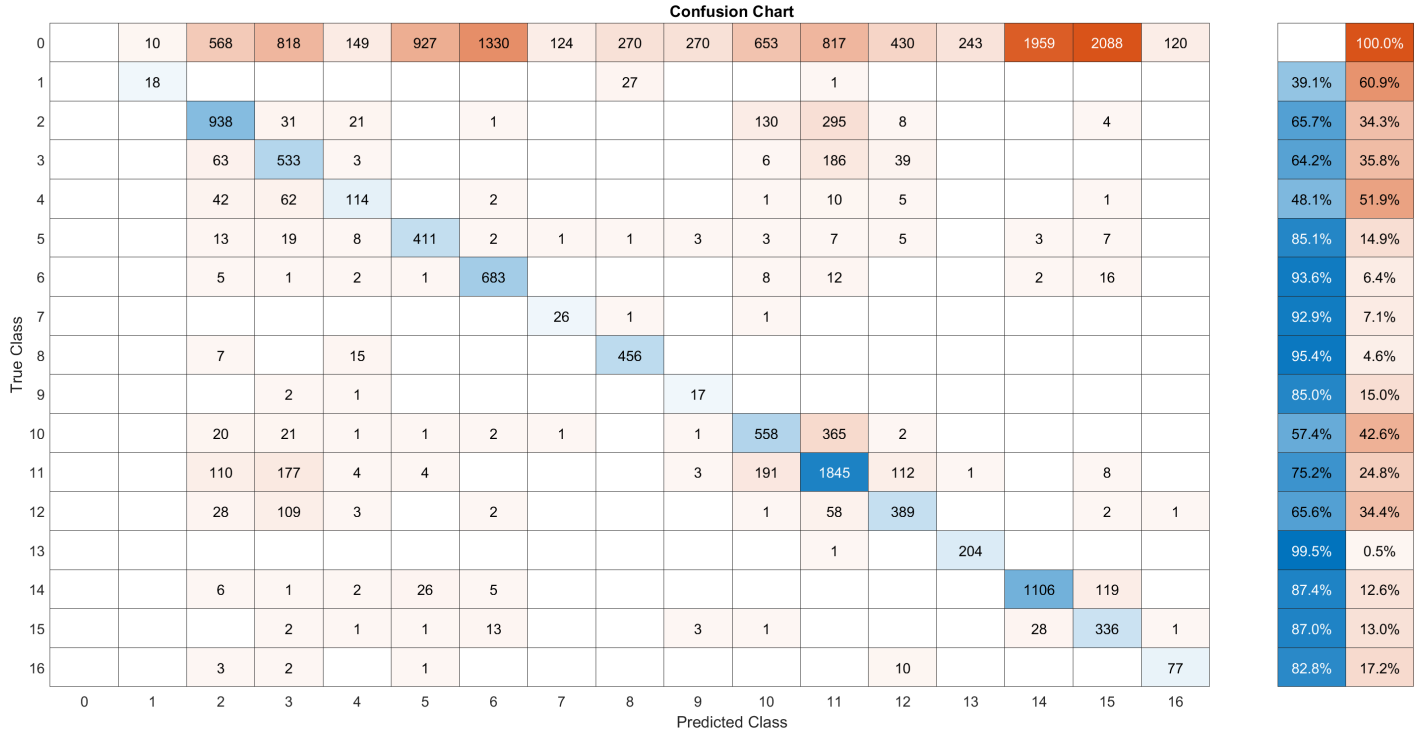


Figure 16: Confusion matrix based on the method of the unknown \mathbf{U}

The absence of values in the first column and the elevated values in the first row are explained in the same way as the other two techniques and will therefore not be repeated. However, when looking at the summarizing table on the right hand side, one can see that the portion of correctly classified pixels is significantly higher than the other two methods. Some classes of the ground truth are still wrongly classified more than they are correctly classified, but this can be due to the imprecision of the calculated endmembers. Moreover, it could be that the algorithm actually detects a certain endmember truthfully when looking at the terrain but that this piece of terrain was classified otherwise (or not classified at all) in the ground truth. This is also a possible source of errors. When looking at the confusion matrix, it is obvious that the approach of the unknown \mathbf{U} gives better classification results than the method of the pseudo-inverse or the optimum detection.

4 Conclusion

In this report, the process of hyperspectral unmixing was described in detail. First, the data at hand, a hyperspectral cube of the Indian Pine site, was elaborated and visually represented. Then, the openly available ground truth was visualized and discussed. Afterwards, the data was exploited. On the one hand, several methods for the extraction of endmembers were qualitatively described and compared to a reference based on correlation, in particular the algorithms of PPI, N-FINDR and FPPI as well as a last method based on the knowledge of the ground truth. Comparing these approaches lead to the conclusion that the correlation was not a valid metric of comparison, since the endmembers of the reference itself were heavily correlated between each other. Therefore, a choice was made to utilize the endmembers that were calculated based on the ground truth. On the other hand, the abundance of each endmember was calculated using three different approaches. The two first approaches are completely equivalent and produced exactly the same results. For both methods, the calculated abundances were used to classify the scene. This classification was compared to the ground truth and both methods were proven not proficient in performing classification. A third method, based on the calculation of a special filter to determine the endmembers, allowed to obtain rather elevated levels of correct classification. It is therefore concluded that the calculation of an adapted filter is the best approach to determine the abundances of a set of endmembers. Hereby one needs to take into account that the endmembers were obtained using the ground truth, but this will not always be possible for every application. In general, the precision of the endmembers plays a non-negligible role in the accuracy of any approach to calculating the abundance.

A Appendices

A.1 Field Notes Indian Pines (1992)

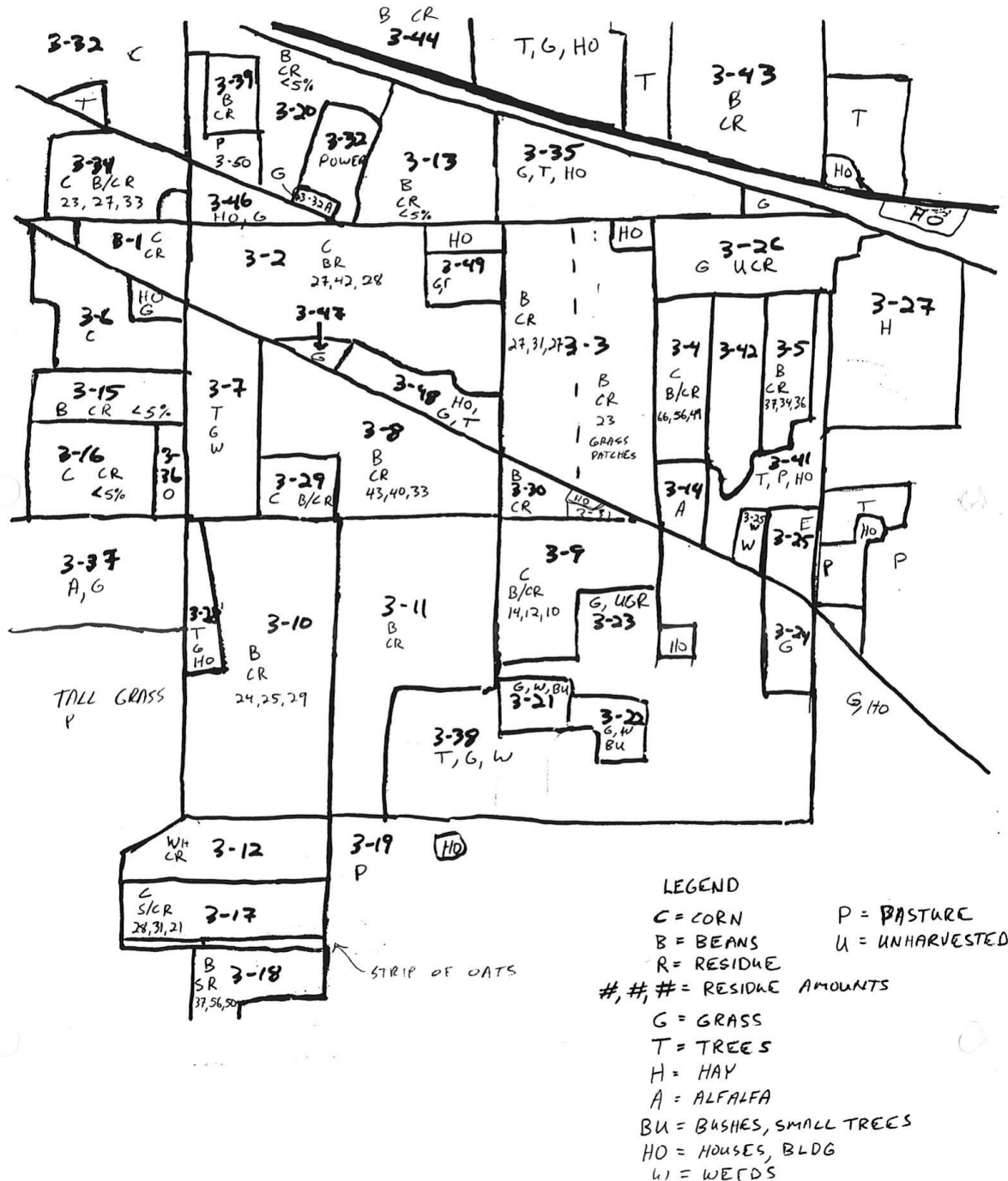


Figure 17: Field notes of the Indian Pines scene

92 site 3 (50,136,27)

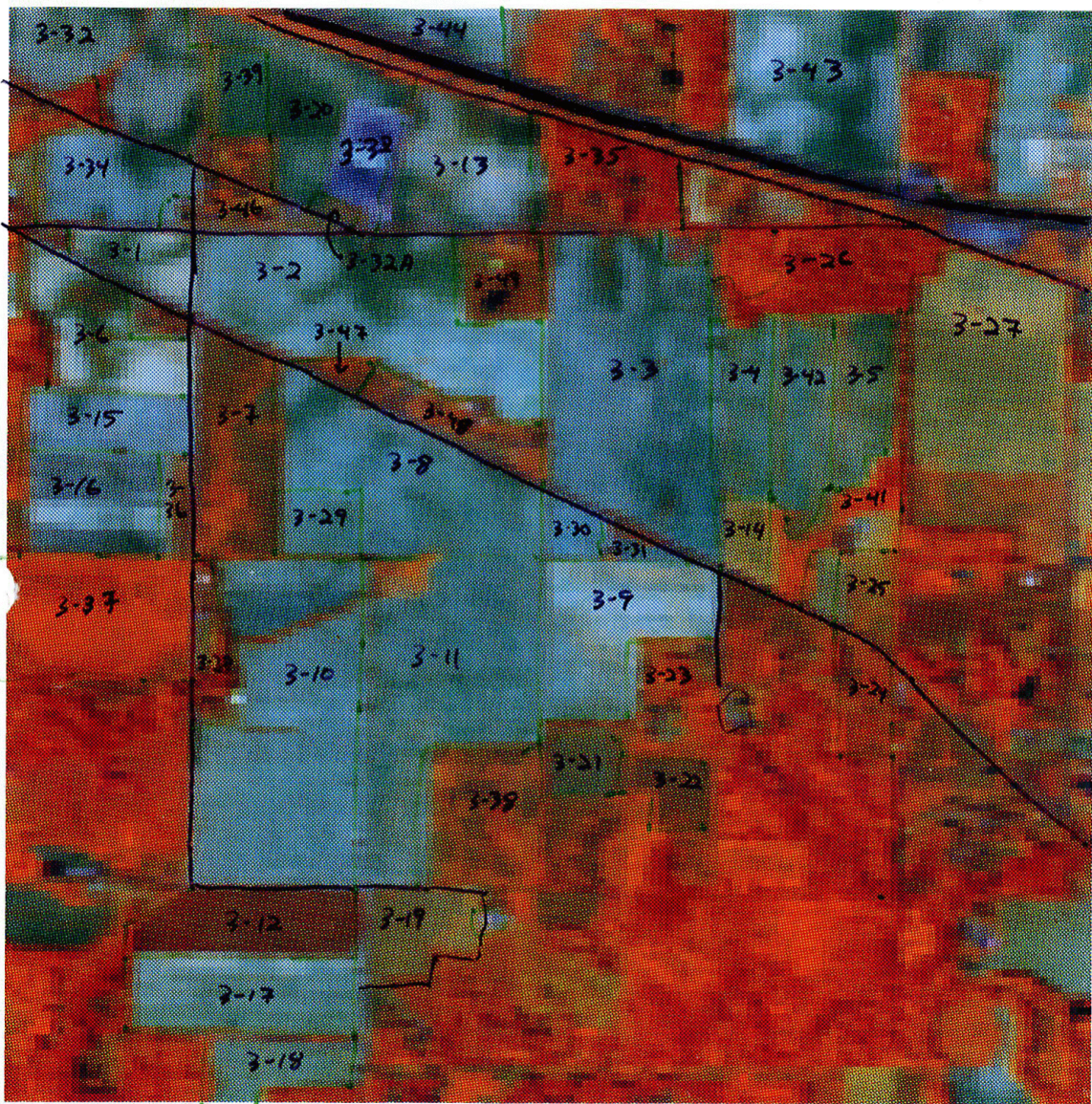


Figure 18: Field notes of the Indian Pines scene

References

- [1] *Aviris - Airborne Visible / Infrared Imaging spectrometer*. URL: <https://aviris.jpl.nasa.gov/>.
- [2] Joseph W. Boardman, Fred A. Kruse, and Robert O. Green. “Mapping target signatures via partial unmixing of AVIRIS data: in Summaries”. In: 1995.
- [3] Chein-I Chang and Qian Du. “Estimation of Number of Spectrally Distinct Signal Sources in Hyperspectral Imagery”. In: *Geoscience and Remote Sensing, IEEE Transactions on* 42 (Apr. 2004), pp. 608–619. DOI: 10.1109/TGRS.2003.819189.
- [4] Chein-I Chang and Qian Du. “Estimation of number of spectrally distinct signal sources in hyperspectral imagery”. In: *IEEE Transactions on Geoscience and Remote Sensing* 42.3 (2004), pp. 608–619. DOI: 10.1109/TGRS.2003.819189.
- [5] Chein-I. Chang and Antonio J. Plaza. “A fast iterative algorithm for implementation of pixel purity index”. In: *IEEE Geoscience and Remote Sensing Letters* 3 (2006), pp. 63–67.
- [6] *Classify Hyperspectral Images Using Deep Learning*. URL: <https://nl.mathworks.com/help/images/hyperspectral-image-classification-using-deep-learning.html>.
- [7] Ben De Schampheleire. *Hyperspectral Unmixing*. Version 1.0.0. Nov. 2022. URL: https://github.com/BenDeSchampheleire/Hyperspectral_Unmixing.
- [8] *Hyperspectral remote sensing scenes*. URL: https://www.ehu.eus/ccwintco/index.php/Hyperspectral_Remote_Sensing_Scenes.
- [9] Larry L. Biehl Marion F. Baumgardner and David A. Landgrebe. *220 Band AVIRIS Hyperspectral Image Data Set: June 12, 1992 Indian Pine Test Site 3*. Sept. 2015. DOI: doi:/10.4231/R7RX991C. URL: <https://purrr.purdue.edu/publications/1947/1>.
- [10] Jose Melian et al. “A novel method to estimate the number of endmembers in hyperspectral images based on the virtual dimensionality concept”. In: *2013 5th Workshop on Hyperspectral Image and Signal Processing: Evolution in Remote Sensing (WHISPERS)*. 2013, pp. 1–4. DOI: 10.1109/WHISPERS.2013.8080620.
- [11] *Pixel Purity Index*. URL: <https://www.l3harrisgeospatial.com/docs/pixelpurityindex.html>.
- [12] Michael E. Winter. “N-FINDR: an algorithm for fast autonomous spectral end-member determination in hyperspectral data”. In: *Optics & Photonics*. 1999.
- [13] Chao-Cheng Wu, Hsian-Min Chen, and Chein-I. Chang. “Real-time N-finder processing algorithms for hyperspectral imagery”. In: *Journal of Real-Time Image Processing* 7 (2010), pp. 105–129.